RSC Advances

ROYAL SOCIETY OF CHEMISTRY

www.rsc.org/advances

Cite this: DOI: 10.1039/c0xx00000x

www.rsc.org/xxxxxx

ARTICLE TYPE

Porous and low-defected graphitic carbon nitride nanotubes for efficient hydrogen evolution under visible light irradiation

Zhijun Huang, Fengbo Li,* Bingfeng Chen and Guoqing Yuan*

Received (in XXX, XXX) Xth XXXXXXXXX 20XX, Accepted Xth XXXXXXXXX 20XX

DOI: 10.1039/b000000x

Porous and low-defected graphitic carbon nitride (g-C_3N_4) nanotubes were fabricated through heating precursors synthesized by recrystallization from H_2SO_4/methanol. The textural and chemical structures of the as-prepared samples were well studied. Recrystallization and subsequent heating result in g-C_3N_4 nanotubes with developed porosity and high specific surface area. Unexpectedly, the nanotubes exhibit much ordered tri-*s*-triazine conjugated network and fewer defects. Compared to bulk g-C_3N_4 prepared by direct heating melamine, the nanotubes demonstrate enhanced photocatalytic activity for hydrogen evolution under visible light irradiation. Besides the improved textural and chemical structures, the optimized optical and electronic properties are contributed to the enhanced photocatalytic performance.

1 Introduction

Photocatalytic water splitting is a promising route for the conversion and utilization of solar energy. Since Fujishima and Honda reported the production of hydrogen from water under TiO_2 electrode in 1972, highly efficient photocatalysts have been regarded as a core subject in this field.[1] Recently, graphitic carbon nitride (g-C_3N_4), an organic semiconductor was found to be able to generate hydrogen from water under visible-light irradiation without the assistance of any metal.[2] Due to the low cost, excellent stability, and specific optical and electronic properties, g-C_3N_4 has attracted impressive attention and has been widely used in water splitting,[3] pollutants photodegradation,[4] CO_2 photoreduction[5] and organic photosynthesis[6].

Traditionally, g-C_3N_4 can be synthesized facilely by self-condensation of nitrogen-rich precursors, such as cyanamide, dicyanamide or melamine.[7] However, the specific surface area of the prepared g-C_3N_4 is very low, normally below 10 $m^2 g^{-1}$.[8] For catalysts, the lower specific surface area means the fewer surface catalytic active sites, which may result in a poor catalytic performance. A number of techniques for increasing the specific surface area have been explored, such as thermal oxidation etching,[9] liquid exfoliation,[10,11] protonation,[12] loading[13,14] and so on. Among various techniques, the introduction of porosity in bulk g-C_3N_4 is the most efficient and wildly used method.[15] For example, a class of mesoporous g-C_3N_4 was prepared by nanocasting method using colloidal silica spheres or mesoporous silica as hard templates.[16-18] By adjusting the mass ratio of precursor to template, a high BET surface area (S_{BET}) of 440 $m^2 g^{-1}$ was achieved.[16] However, nanocasting technology is not suitable for large-scale applications, because removal of templates is not only time consuming but also environmentally unfriendly. Alternatively, soft templates can also be used to prepare porous g-C_3N_4. By special selection of templates (surfactants or ionic liquids) and careful controlling polymerization conditions, porous g-C_3N_4 materials were synthesized successfully.[19-21] Whereas, using soft templates for the preparation of porous g-C_3N_4 is uneconomical. In addition, carbon or heteroatom residues derived from the templates may be left in the resulting photocatalysts, which may act as defects and increase the lattice disorder of g-C_3N_4.[22]

It is well known that defects play an important role in influencing the photocatalytic performance of g-C_3N_4. Defects may benefit to the photocatalytic activity by broadening the light responsive range and facilitating the charge separation.[23,24] On the other hand, defects such as NH/NH_2 groups result from the incomplete condensation could serve as recombination centers for photo-generated charges, which reduce the free carrier concentration and deteriorate the catalytic efficiency.[25] Therefore, eliminating these defects is a promising route to improve the photocatalytic performance of g-C_3N_4. However, only few studies have been focused on this issue.[26]

Very recently, bulk g-C_3N_4 was dissolved in concentrated H_2SO_4 by Zhang and co-workers.[27] A surprisingly high concentration of 300 mg/mL was obtained. By recrystallization of g-C_3N_4 from solution, thin-film electrodes,[28] ultrathin nanosheets[29] and nano-size g-C_3N_4 [30] have been fabricated respectively. Herein, we fabricate porous g-C_3N_4 nanotubes through heating precursors derived from a similar but modified recrystallization strategy. Compared to bulk g-C_3N_4 prepared by direct heating melamine, the as-prepared g-C_3N_4 nanotubes exhibit well developed porosity and larger S_{BET} (117.7 $m^2 g^{-1}$). Surprisingly, except for the textural superiority, this photocatalytic material exhibits higher polymerization degree, fewer defects, and improved optical and electronic properties. The catalytic performance of the porous g-C_3N_4 nanotubes were evaluated by photocatalytic water

splitting under visible-light irritation, and compared with that of g-C_3N_4 prepared from melamine.

2 Experimental

2.1 Chemicals

Melamine (99%) was purchased from Aladdin. Concentrated H_2SO_4 (98%) was purchased from Sinopharm Chemical Reagent Corp, PR China. All the solvents are analytical grade agents and purchased from Aladdin without further purification.

2.2 Preparation of catalysts

Bulk g-C_3N_4 (BCN) was prepared by direct heating melamine at 550 ^oC for 2 h in still air. The heating rate was 10 °C min^{-1}. After cooled to room temperature, BCN was ground to a homogeneous powder. 3 g BCN was stirred with 30 mL concentrated H_2SO_4 at 60 ^oC for 30 minutes. 30 mL deionized water was added to the suspension within 1 min. The temperature was increased rapidly to about 100 °C and BCN was dissolved to form a transparent solution. This solution was added to 1500 mL methanol slowly with stirring. A white precipitate was formed. After cooled to room temperature, the precipitate was collected by centrifugation, washed thoroughly with water and ethanol, and dried at 60 °C for 24 hours. The obtained white product was marked as CNS. Porous g-C_3N_4 nanotubes were prepared by heating CNS at 550 ^oC for 2 h in still air with a heating rate of 5 °C min^{-1}. The obtained yellow power was marked as CNS-550.

2.3 Catalyst characterization

Scanning electron microscopy (SEM) images were recorded on a Hitachi S-4800 instrument. Transmission electron microscopy (TEM) images were obtained on a JEOL JSM-2100 instrument. Nitrogen adsorption–desorption experiment was performed at 77.3 K by a Quanta-chrome Autosorb Automated Gas Sorption System (Quantachrome Corporation). Before experiments, the samples were dried at 300 ℃ under vacuum for 6 h. Powder X-ray diffraction (XRD) were performed on a Rigaku Rotaex diffractometer equipped with Cu Kα radiation source (40 kV, 200 mA; λ=1.54056 Å). Thermogravimetric analysis (TGA) was performed on a Pyris 1 TGA (Perkin Elmer) at a heating rate of 10 ℃ min^{-1} in nitrogen flux. Fourier transform infrared (FT-IR) spectra were recorded on a Bruker Tensor 27 by using KBr pellets. Elemental analysis (EA) experiments were performed on a Flash EA 1112. X-ray photoelectron spectroscopy (XPS) dates were collected on a Thermo Scientic ESCALab 250Xi using 200 W monochromated Al Kα radiation. UV-visible absorption spectra were obtained using a Shimadzu UV-2600 UV-visible spectrometer equipped with an integrating sphere assembly. $BaSO_4$ was used as reference. Photoluminescence (PL) spectra were recorded on a Hitachi F-4500 fluorescence spectrometer with excitation at 320 nm. Time-resolved fluorescence experiments were performed on an Edinburgh FLES920. Electron paramagnetic resonance (EPR) measurements were carried out on a Bruker E500 spectrometer at room temperature.

2.4 Photocatalytic activity test

Photocatalytic hydrogen evolution reactions were performed in a quartz reactor. Typically, 50 mg photocatalysts were dispersed in an aqueous solution (100 mL) containing triethanolamine (10 vol%, sacrificial reagent) and H_2PtCl_6. Pt (3 wt%, co-catalyst) was in-situ photo-deposited onto g-C_3N_4 under light irradiation. Prior to irradiation, the suspension was purged with N_2 for 30 minutes to remove air. The light was provided by a 300 W Xe lamp with cut off filter (λ > 420 nm). The temperature was maintained at 25 °C by the flow of cooling water during the irradiation. The produced hydrogen was analyzed by a gas chromatography (GC-2014, Shimadzu) equipped with a thermal conductive detector (TCD).

3 Results and discussion

3.1 Textural and chemical structures of porous g-C_3N_4 nanotubes

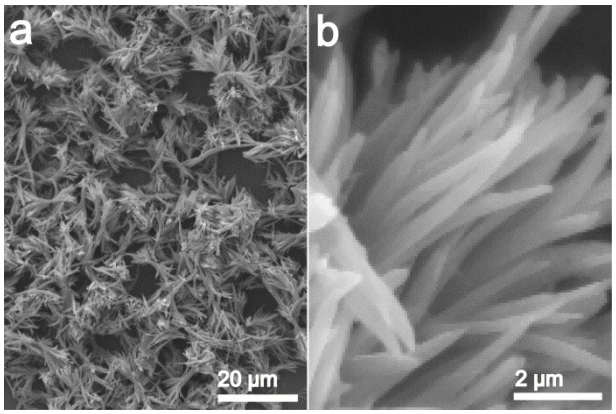

Figure 1 SEM images of CNS with different magnifications.

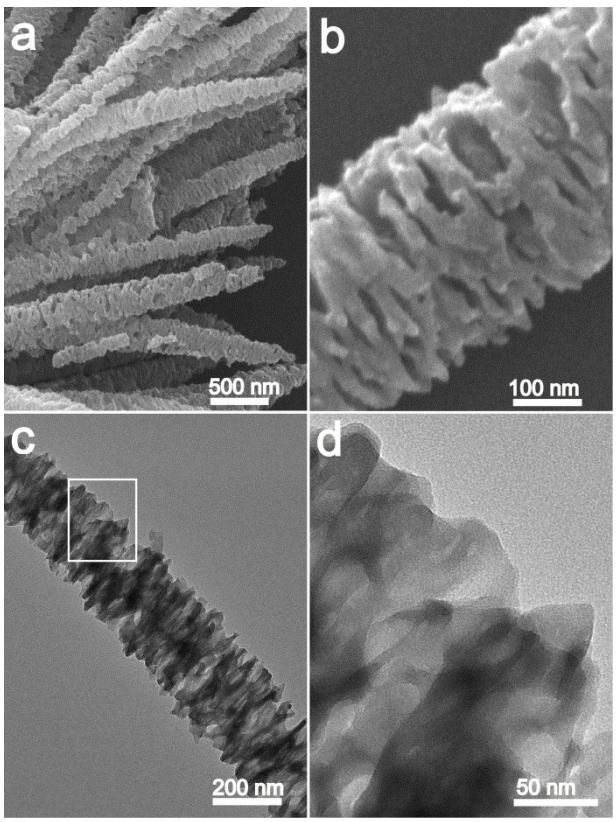

Figure 2 SEM (a, b) and TEM (c, d) images of CNS-550. Picture (d) corresponds to the enlarged areas of white rectangle in (c).

Previous studies revealed that g-C_3N_4 prepared by direct heating melamine are bulk morphology with several micrometers in size.[31] While it is dissolved in H_2SO_4, BCN is exfoliated into single atomic layer nanosheets. The nanosheets are then rearranged to nanorods during recrystallization with methanol. It can be seen from Figure 1 that these nanorods are reassembled into a flower-like morphology. The diameters of the nanorods are about 300–400 nm and the lengths are about the order of several micrometers. The effects of solvents on the morphology of the products were also studied. When performing the recrystallization experiments with other orgnic solvents (ethanol, ethylene glycol, acetonitrile, acetone, dimethyl sulfoxide, N,N-dimethylformamide and N-methyl pyrrolidone), regularly shaped precipitates could not be formed. Concentration also affects the morphology of the obtained smaples. The best result only can be achieved at a concentration of about 2 mg mL^{-1}. It is clear that solvent conditions have a great impact on the morphology of CNS.

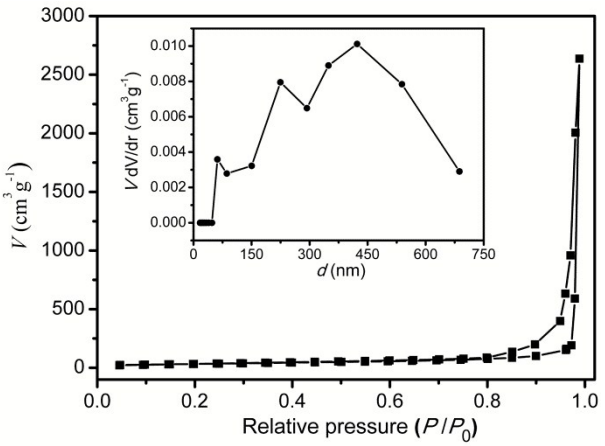

Figure 3 Nitrogen adsorption–desorption isotherm and BJH pore size distribution curve (inset) of CNS-550.

Heating CNS at 550 °C for 2 hours yields porous g-C_3N_4 nanotubes (CNS-550). As shown in Figure 2a, the as-prepared samples after heating inherit the rod-like structures. The inner part of CNS undergoes serious structural shrinkage, resulting in hollow nanotubes consisting of curly nanosheets (Figure 2b). Numerous macropores of 50–100 nm are embedded in the nanosheets. The porous structure is further confirmed by TEM measurements. A nanotube of about 250 nm in diameter with developed porosity is imaged in Figure 2c. From the high-resolution TEM image (Figure 2d) of the detailed local structure of CNS-550, distinct layered nanosheets are obseved clearly. It can be expected reasonably that the nanosheet structure and developed porosity are not only useful for providing more catalytic active sites, but also helpful for adsorption and diffusion of reactants during photocatalytic reactions.[32]

The textural information of CNS-550 was analyzed by nitrogen adsorption–desorption experiment. In Figure 3, a typical type III isotherm is observed. The H3 hysteresis loop located at 0.80 < P/P_0 < 1.00 supports the SEM and TEM results that macroporous structure exists in the photocatalyst. The sizes of the pores are above 50 nm as demonstrated by the Barrett-Joyner-Halenda (BJH) pore size distribution curve (Figure 3, inset). The S_{BET} was calculated to be 117.7 $m^2 g^{-1}$. For comparison, the S_{BET} of BCN and CNS were determined to be 10.6 and 31.3 $m^2 g^{-1}$ respectively, much lower than that of CNS-550.

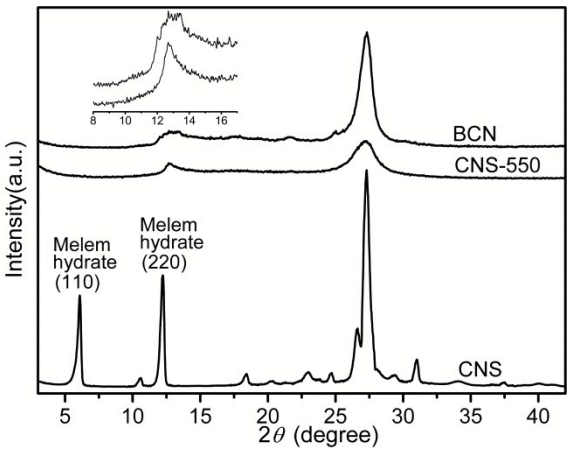

Figure 4 XRD patterns of BCN, CNS and CNS-550.

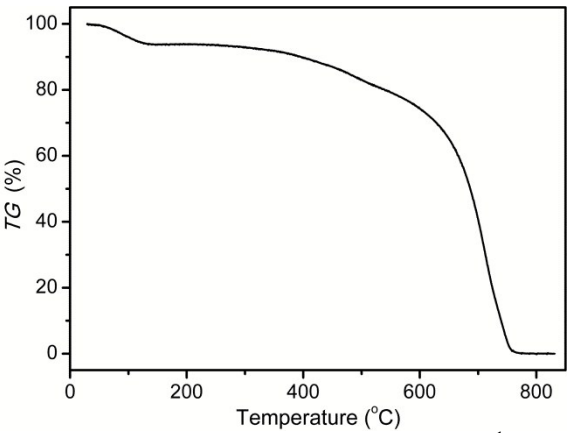

Figure 5 TGA of CNS at a heating rate of 10 °C min^{-1} under N_2 flux.

The crystal structures of the smaples were investigated by power XRD (Figure 4). BCN displays a characteristic diffraction peak at 27.3°, which corresponds to the interlayer-stacking structures (002). This peak becomes sharper and stronger after treated with H_2SO_4, indicating a higher crystallinity was achieved. A broad and weak peak at 13.1°, which is ascribed to the in-planar repeating tri-*s*-triazine units (100), is also appeared in the XRD pattern of BCN. This peak is overlapped with a strong and sharp peak at 12.2° for CNS. Another peak located at 6.1° is also observed for CNS. These two peaks are in good agreement with the (220) and (110) characteristic peaks of melem hydrate.[33,34] It is believed that bulk g-C_3N_4 is typically synthesized by polymerization of nitrogen-rich precursors at high-temperature through a solid-solid reaction process. During the reactions, a large amount of intermediates are generated and interact with the formed g-C_3N_4 through hydrogen bonds. As a result, these intermediates cannot be polymerized completely. These unstable and not-well-ordered components could be hydrolyzed during hydrothermal process.[35,36] According to the XRD results, we speculate that the intermediates in g-C_3N_4 derived from the incomplete polymerization were dissociated into melem.

The generation of melem was further confirmed by TGA analysis.

As shown in Figure 5, the TGA curve of CNS shows a marked weight loss below 140 °C, which corresponds to the dehydration. A moderate loss of weight starts at about 400 °C, indicating the polymerization of melem occurred.[37] The as-generated g-C_3N_4 materials begin to decompose at about 550 °C, which is consistent with the literatures.[9,38]

The crystal structure of CNS was changed after heating. As demonstrated by Figure 4, the XRD pattern of CNS-550 restores to substantially the same as that of BCN except for some minor changes. The characteristic peaks of melem hydrate disappeared due to the dehydration and polymerization. Compared to BCN, CNS-550 exhibits a less pronounced (002) peak. This can be explained by the reduced thickness of the nanosheets and the introduction of porosity in CNS-550.[4,10] However, the similar result does not appear for (100) peak. From the XRD patterns (Figure 4, inset), the (100) peak of CNS-550 becomes sharper and shifts to a lower angle of 12.8°. This indicates that CNS-550 has a higher crystallinity and improved tri-s-triazine conjugated network. In other words, the defects which disturb the periodicity in the direction parallel to the tri-s-triazine layer are eliminated during dissolution, recrystallization and heating.

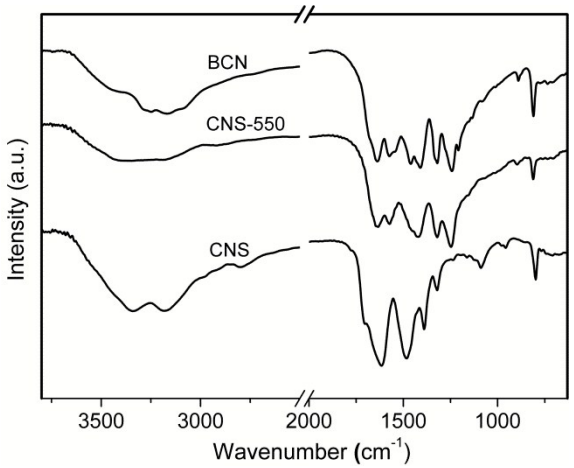

Figure 6 FT-IR patterns of BCN, CNS and CNS-550.

Table 1 EA results of BCN, CNS and CNS-550.

Smaples	C (wt%)	N (wt%)	H (wt%)	O (wt%)	C/N [a]
BCN	34.23	60.66	1.98	3.13	0.66
CNS	30.23	53.87	3.76	12.14	0.65
CNS-550	35.60	60.66	1.62	2.12	0.68

[a] atomic ratio

The chemical compositions of CNS and CNS-550 were investigated by FT-IR, EA and XPS measurements. FT-IR spectrum of CNS in Figure 6 shows a typical characteristic band of *s*-triazine ring at 799 cm^{-1}. This suggests that the core chemical structure of g-C_3N_4 is rather stable against H_2SO_4.[27] Five absorption bands with different intensities at 1241, 1321, 1390, 1438 and 1616 cm^{-1} are originated from the C-N stretches and N-H bending vibrations. The weak absorption band at 1089 cm^{-1} may be stemmed from the protonation of g-C_3N_4.[30] Two broad absorption bands centered at 3183 and 3340 cm^{-1} indicate the existence of amino and hydroxyl groups, which are mainly derived from melem hydrate.[39] Heating CNS at 550 °C, melem was condensed into g-C_3N_4. As a result, CNS-550 exhibits a typical FT-IR pattern of g-C_3N_4. Structural defects affect FT-IR spectra slightly. CNS-550 with fewer defects (NH/NH_2) than that of BCN exhibits weaker absorption in the N–H stretching region between 3000 and 3500 cm^{-1}.

EA dates show a similar result as that of FT-IR spectra. As summarized in table 1, the H and O contents of BCN is 1.98 and 3.13 wt% respectively. These values are increased to 3.76 and 12.14 wt% for CNS due to the incorporation of H_2O. The C/N atomic ratio is increased from 0.66 for BCN to 0.68 for CNS-550. This is ascribed to the elimination of defects with lower C/N atomic ratio during recrystallization and polymerization at high temperature. For the same reason, CNS-550 shows a lower H content compared to BCN.

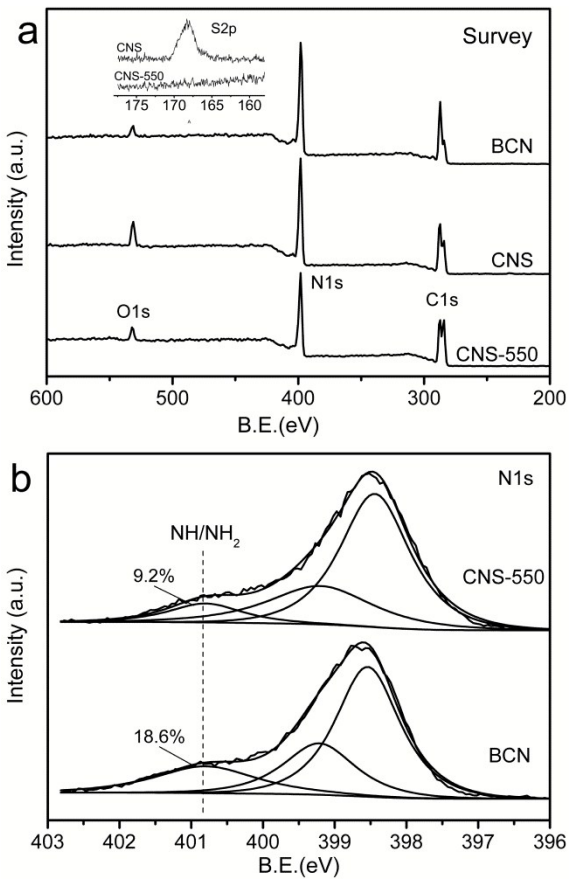

Figure 7 (a) XPS survey spectra of BCN, CNS and CNS-550. (b) N1s XPS peaks of CNS and CNS-550.

From the XPS survey spectra (Figure 7a), it is seen that the all the samples are mainly composed of C, N and O elements. For CNS, C and N are ascribed to g-C_3N_4 and melem. According to the XRD results, O is stemmed from the adsorbed H_2O, which is connected with melem through hydrogen bonds. It should be noted that a small amount of S is also detected in CNS (Figure 7a, inset). The high-resolution S2p spectrum shows a binding energy of 168.2 eV, which is consistent with the energies characteristic of SO_4^{2-} The incorporation of SO_4^{2-} indicates the effective protonation of g-C_3N_4 during dissolution with H_2SO_4. The residual S can be removed thoroughly by heating at 550 °C, which is in agreement with the literature.[40]

The structural defects are reflected by N1s XPS spectra. As

shown in Figure 7b, the N1s spectra of CNS and CNS-550 are fitted into three peaks at 400.9, 399.6 and 398.4 eV, corresponding to NH/NH_2, $N–(C)_3$ and C–N=C respectively.[41,42] The content of N in NH/NH_2 (defects) for BCN is 18.6%. Due to the elimination of defects, this value is decreased largely to 9.2% for CNS-550.

3.2 Optical and electronic properties of porous g-C_3N_4 nanotubes

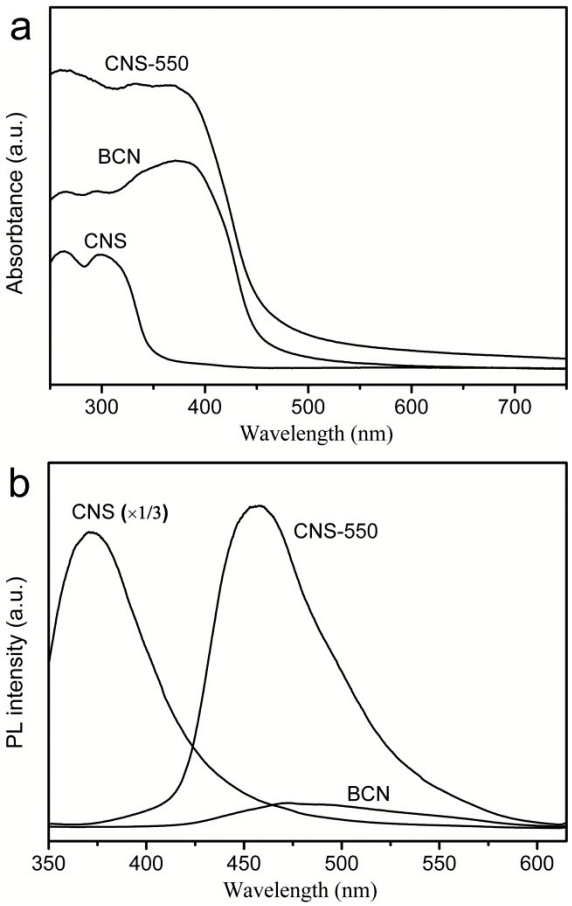

Figure 8 UV-visible absorption spectra (a) and PL spectra (b) of BCN and CNS-550.

Textural and chemical structures affect the optical and electronic properties of g-C_3N_4 significantly. As shown in Figure 8a, BCN demonstrates an absorption edge of about 450 nm. The absorption edge of CNS shifts markedly to about 340 nm due to the protonation. A slightly red-shifted optical absorption edge is observed for CNS-550. Therefore, more visible light can be utilized. It should be noted that, compared to bulk g-C_3N_4, g-C_3N_4 nanocomposites generally exhibit a blue-shifted absorption edge due to the quantum confinement. For CNS-550, the improved polymerization degree narrows the bandgap and broadens the visible-light responsive range.[34] An obviously increased absorption intensity is observed for CNS-550 in UV range, which is probably due to the quantum confinement and the multiple reflections of light within the porous structure.[43,44]

Textural and chemical structure-induced optical and electronic propertis improvment was further investigated by PL spectra. Figure 8b shows a strong PL emission peak centered at 455 nm for BCN. The PL emission is originated from the recombination of photo-generated electron–hole pairs.[45] The emission peak of CNS is blue shifted to about 370 nm, which is in agreement with its UV-visible absorption. A significantly decreased PL intensity is observed for CNS-550, which means that the recombination of electron–hole pairs was suppressed largely. As a result, the efficiency for the utilization of the absorbed light improved. Two reasons are responsible for this improvement. First, the increase in the crystallinity could decrease the recombination center concentration.[25] Second, the thin thickness of the nanosheets may shorten the transportation length of photogenerated charge. [11]

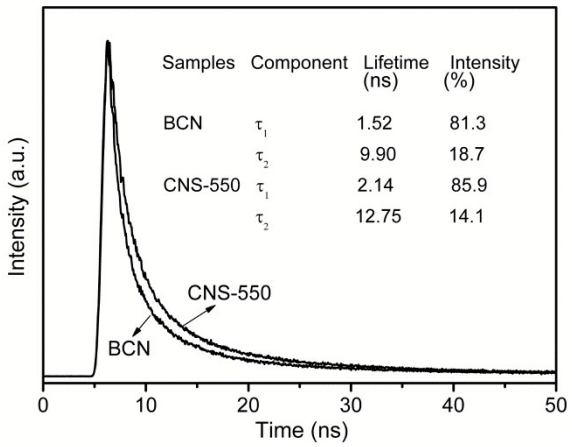

Figure 9 Time-resolved fluorescence decay spectra of BCN and CNS-550.

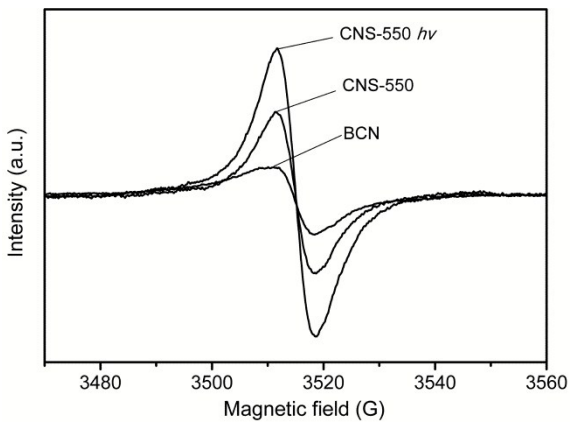

Figure 10 EPR spectra of BCN and CNS-550 in the dark or under light irradation.

The improved efficiency in the transfer of charge carriers was also examined by time-resolved fluorescence spectra. As shown in Figure 9, the spectra of BCN and CNS-550 are well fit to double-exponential decay model. The lifetimes and the corresponding fractional contributions are summarized. CNS-550 displays an obviously prolonged lifetime. The shorter lifetime is increased from 1.52 ns for BCN to 2.14 ns for CNS-550 and the longer lifetime is increased from 9.90 ns for BCN to 12.75 ns for CNS-550. The prolonged lifetime means more photo-generated charge could reach the surface of the photocatalyst and be captured by reactive substrates.[46]

The improved electronic property of CNS-550 was further investigated by room-temperature EPR. As shown in Figure 10,

only one symmetrical single Lorentzian line is observed in both BCN and CNS-550. The *g* value of 2.0034 is in agreement with the lone pair electrons of carbon atoms in tri-*s*-triazine units.[47] Compared with BCN, the EPR intensity of CNS-550 is much stronger, which is attributed to the larger specific surface area. The EPR intensity is further enhanced largely under light irradiation by a 100 W Hg lamp, indicating that a large amount of radicals are generated in the photocatalyst.

3.1 Enhanced photoactivity of porous g-C_3N_4 nanotubes

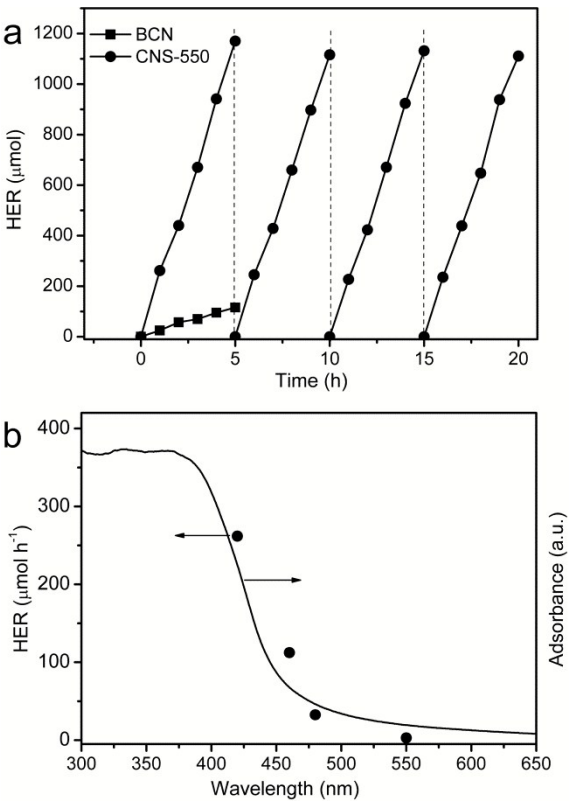

Figure 11 (a) Photocatalytic activities of BCN and CNS-550. (b) Wavelength-dependent photocatalytic activities of CNS-550.

Considering the high S_{BET}, developed porosity, improved chemical structure, and optimized optical and electronic properties, CNS-550 must be significantly favorable for application as a photocatalyst. The photocatalytic activity of CNS-550 was evaluated by the photocatalytic hydrogen evolution under visible light irradiation ($\lambda > 420$ nm). Triethanolamine and 3 wt% Pt are used as the sacrificial reagent and co-catalyst respectively. As shown in Figure 11a, BCN shows a moderate visible light photocatalytic activity. The hydrogen evolution rate (HER) is 24.6 μmol h^{-1}. The catalytic activity of CNS-550 is much higher. A HER of 261.8 μmol h^{-1} is achieved, which is more than 10 times higher than that of BCN. The high polymerization degree provides CNS-550 with excellent stability for the photocatalytic reactions. The production of H_2 increases steadily within 5 hours in the first run. A total amount of 1170.2 μmol hydrogen is produced. This value decreases slightly to 1110.8 μmol for the fourth run. The effect of wavelength on the HER is also investigated. As shown in Figure 11b, the photocatalytic activity of CNS-550 matchs its optical absorption well. The longest wavelength capable for production of hydrogen is about 550 nm. Further increase in the wavelength, hydrogen cannot be produced steadily. This indicates that light shorten than 550 nm can be utilized by CNS-550. It is shown in Figure 8a that no visible light can be absorbed by CNS. As a result, no detectable HER is observed for CNS under visible light irradiation.

Conclusions

In summary, this work has demonstrated an efficient strategy for fabricating porous and low-defected g-C_3N_4 nanotubes through heating precursor derived from recrystallization. Unstable and not-well-ordered components with large amount of defects originated from the incomplete polymerization are dissociated into melem during dissolution and simultaneous hydrolysis. Heating the products precipitated from the solution yields low-defected g-C_3N_4 nanotubes with developed porosity. Associated with the high S_{BET}, developed porosity, lowered defects concentration, and optimized optical and electronic properties, the as-prepared photocatalysts exhibit enhanced photocatalytic activity for hydrogen evolution under visible light irradiation. We hope that our results may lead researchers a new line of thinking for the fabrication of g-C_3N_4 based photocatalyst with modulated physicochemical properties and high activity.

Acknowledgements

This work was supported by the National Natural Science Foundation of China (21304101, 21174148, 21403248, 21373234).

Notes and references

Beijing National Laboratory of Molecular Sciences, Key Laboratory of Green Printing, Institute of Chemistry, Chinese Academy of Sciences, Beijing, PR China. E-mail: lifb@iccas.ac.cn; yuangq@iccas.ac.cn; Fax: +86 10 62559373

1. A. Fujishima and K. Honda, *Nature*, 1972, **238**, 37-38.
2. X. Wang, K. Maeda, A. Thomas, K. Takanabe, G. Xin, J. M. Carlsson, K. Domen and M. Antonietti, *Nat. Mater.*, 2009, **8**, 76-80.
3. S. Cao and J. Yu, *J. Phys. Chem. Lett.*, 2014, **5**, 2101-2107.
4. Z. Huang, F. Li, B. Chen and G. Yuan, *RSC Adv.*, 2015, **5**, 14027-14033.
5. R. Kuriki, K. Sekizawa, O. Ishitani and K. Maeda, *Angew. Chem., Int. Ed.*, 2015, **54**, 2406-2409.
6. Y. Zheng, J. Liu, J. Liang, M. Jaroniec and S. Z. Qiao, *Energy Environ. Sci.*, 2012, **5**, 6717-6731.
7. A. Thomas, A. Fischer, F. Goettmann, M. Antonietti, J.-O. Müller, R. Schlögl and J. M. Carlsson, *J. Mater. Chem.*, 2008, **18**, 4893-4908.
8. Y. Wang, X. Wang and M. Antonietti, *Angew. Chem., Int. Ed.*, 2012, **51**, 68-89.
9. P. Niu, L. Zhang, G. Liu and H.-M. Cheng, *Adv. Funct. Mater.*, 2012, **22**, 4763-4770.
10. X. Zhang, X. Xie, H. Wang, J. Zhang, B. Pan and Y. Xie, *J. Am. Chem. Soc.*, 2013, **135**, 18-21.
11. S. Yang, Y. Gong, J. Zhang, L. Zhan, L. Ma, Z. Fang, R. Vajtai, X. Wang and P. M. Ajayan, *Adv. Mater.*, 2013, **25**, 2452-2456.
12. Y. J. Zhang, A. Thomas, M. Antonietti and X. C. Wang, *J. Am. Chem. Soc.*, 2009, **131**, 50-51.

13. X. F. Chen, J. S. Zhang, X. Z. Fu, M. Antonietti and X. C. Wang, *J. Am. Chem. Soc.*, 2009, **131**, 11658-11659.
14. Z. Huang, F. Li, B. Chen, T. Lu, Y. Yuan and G. Yuan, *Appl. Catal., B*, 2013, **136-137**, 269-277.
15. L. Shi, L. Liang, F. X. Wang, M. S. Liu, T. Liang, K. L. Chen and J. M. Sun, *RSC Adv.*, 2015, **5**, 63264-63270.
16. F. Goettmann, A. Fischer, M. Antonietti and A. Thomas, *Angew. Chem., Int. Ed.*, 2006, **45**, 4467-4471.
17. F. Goettmann, A. Thomas and M. Antonietti, *Angew. Chem., Int. Ed.*, 2007, **46**, 2717-2720.
18. J. S. Zhang, F. S. Guo and X. C. Wang, *Adv. Funct. Mater.*, 2013, **23**, 3008-3014.
19. H. Yan, *Chem. Commun.*, 2012, **48**, 3430-3432.
20. Y. Wang, J. Zhang, X. Wang, M. Antonietti and H. Li, *Angew. Chem., Int. Ed.*, 2010, **49**, 3356-3359.
21. K. Kailasam, J. D. Epping, A. Thomas, S. Losse and H. Junge, *Energy Environ. Sci.*, 2011, **4**, 4668.
22. J. Luo, X. S. Zhou, L. Ma and X. Y. Xu, *RSC Adv.*, 2015, **5**, 68728-68735.
23. Y. Cui, G. Zhang, Z. Lin and X. Wang, *Appl. Catal., B*, 2016, **181**, 413-419.
24. H. Q. Ma, S. Zhao, S. Li and N. Liu, *RSC Adv.*, 2015, **5**, 79585-79592.
25. P. Wu, J. Wang, J. Zhao, L. Guo and F. E. Osterloh, *J. Mater. Chem. A*, 2014, **2**, 20338-20344.
26. Q. Lin, L. Li, S. Liang, M. Liu, J. Bi and L. Wu, *Appl. Catal., B,* 2015, **163**, 135-142.
27. Z. Zhou, J. Wang, J. Yu, Y. Shen, Y. Li, A. Liu, S. Liu and Y. Zhang, *J. Am. Chem. Soc.*, 2015, **137**, 2179-2182.
28. J. Zhang, M. Zhang, L. Lin and X. Wang, *Angew. Chem., Int. Ed.*, 2015, **54**, 6297-6301.
29. X. Du, G. Zou, Z. Wang and X. Wang, *Nanoscale*, 2015, **7**, 8701-8706.
30. Y. Xu, M. Xie, S. Huang, H. Xu, H. Ji, J. Xia, Y. Li and H. Li, *RSC Adv.*, 2015, **5**, 26281-26290.
31. Z. Huang, F. Li, B. Chen and G. Yuan, *Catal. Sci. Technol.*, 2014, **4**, 4258-4264.
32. J. Zhang, M. Zhang, C. Yang and X. Wang, *Adv. Mater.*, 2014, **26**, 4121-4126.
33. S. J. Makowski, P. Kostler and W. Schnick, *Chem. Eur. J.*, 2012, **18**, 3248-3257.
34. V. W. Lau, M. B. Mesch, V. Duppel, V. Blum, J. Senker and B. V. Lotsch, *J. Am. Chem. Soc.*, 2015, **137**, 1064-1072.
35. T. Sano, S. Tsutsui, K. Koike, T. Hirakawa, Y. Teramoto, N. Negishi and K. Takeuchi, *J. Mater. Chem. A*, 2013, **1**, 6489.
36. L. Ming, H. Yue, L. Xu and F. Chen, *J. Mater. Chem. A*, 2014, **2**, 19145-19149.
37. B. V. Lotsch, M. Doblinger, J. Sehnert, L. Seyfarth, J. Senker, O. Oeckler and W. Schnick, *Chem. Eur. J.*, 2007, **13**, 4969-4980.
38. G. Zhang, J. Zhang, M. Zhang and X. Wang, *J. Mater. Chem.*, 2012, **22**, 8083.
39. E. Wirnhier, M. B. Mesch, J. Senker and W. Schnick, *Chem. Eur. J.*, 2013, **19**, 2041-2049.
40. J. Xu, Y. Wang and Y. Zhu, *Langmuir*, 2013, **29**, 10566-10572.
41. D. J. Martin, K. P. Qiu, S. A. Shevlin, A. D. Handoko, X. W. Chen, Z. X. Guo and J. W. Tang, *Angew. Chem., Int. Ed.*, 2014, **53**, 9240-9245.
42. J. Liu, Y. Liu, N. Y. Liu, Y. Z. Han, X. Zhang, H. Huang, Y. Lifshitz, S. T. Lee, J. Zhong and Z. H. Kang, *Science*, 2015, **347**, 970-974.
43. J. Sun, J. Zhang, M. Zhang, M. Antonietti, X. Fu and X. Wang, *Nat. Commun.*, 2012, 1139.
44. J. Mao, T. Peng, X. Zhang, K. Li, L. Ye and L. Zan, *Catal. Sci. Technol.*, 2013, **3**, 1253.
45. Z. F. Huang, J. J. Song, L. Pan, Z. M. Wang, X. Q. Zhang, J. J. Zou, W. B. Mi, X. W. Zhang and L. Wang, *Nano Energy*, 2015, **12**, 646-656.
46. M. Shalom, S. Inal, C. Fettkenhauer, D. Neher and M. Antonietti, *J. Am. Chem. Soc.*, 2013, **135**, 7118-7121.
47. G. Zhang and X. Wang, *J. Catal.* 2013, **307**, 246-253.

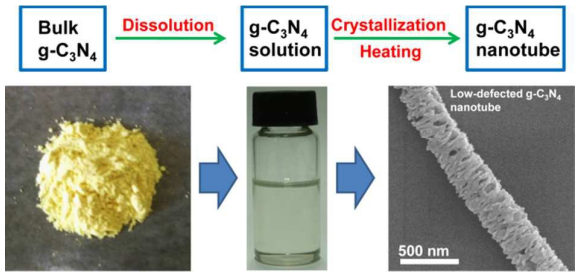

Porous and low-defected g-C_3N_4 nanotubes with high S_{BET} and optimized optical and electronic properties exhibit enhanced photocatalytic activity.